Effects of Basicity and Al$_2$O$_3$ Content on the Chemistry of Phases in Iron Ore Sinter Containing ZnO

JUNWOO PARK, RAMARAGHAVULU RAJAVARAM, IN-KOOK SUH, JIWON JEON, SANGHAN SON, and JOONHO LEE

The effects of basicity and Al$_2$O$_3$ content on the chemistry of phases in iron ore sinter containing ZnO were investigated by Rietveld analysis of the X-ray diffraction (XRD) patterns. Bulk composition analysis was carried out using inductively coupled plasma-atomic emission spectroscopy (ICP-AES) and wet-chemical analysis. The composition of each phase was investigated using a scanning electron microscope-energy dispersive X-ray analyzer (SEM-EDX). It was found that ZnO exists in the franklinite and the silicoferrite of calcium and aluminum (SFCA) phases. With increasing ZnO content, the phase fraction of the franklinite increased, while the fraction of SFCA slightly increased. When ZnO content was fixed at 1 wt pct and basicity increased, the fraction of franklinite decreased and that of SFCA increased. Here, the solubility of ZnO in the SFCA increased. As the Al$_2$O$_3$ content increased, the fraction of franklinite decreased and that of SFCA increased, while ZnO content in the SFCA did not change significantly.

© The Author(s) 2020

I. INTRODUCTION

RECYCLING by-products generated from the integrated iron- and steelmaking industry has drawn attention from the vantage point of environmental and economic issues. Charging of iron-containing industrial by-products, such as scrap and dust in the blast furnace (BF), is useful to reduce CO$_2$ emission from the ironmaking process as well as to increase economic competency.[1–4] For example, BF dust can be considered as a source of iron in BF operation, because it contains 15 to 40 wt pct of Fe. Recycling of BF dust has been generally applied to the sintering process.[5–7] BF dust is mostly composed of carbon, CaO, SiO$_2$, and iron oxides, but it contains some minor constituents such as Al$_2$O$_3$, MgO, ZnO, and so on. Among them, many researchers pointed out that zinc in iron ore sinter may cause accumulation of ZnO in the iron ore sinter and wear of the refractory material during the BF operation.[8–10]

When iron ore sinter containing Zn is charged in the BF, or pulverized coal containing Zn is injected into the BF through tuyere nozzles, Zn vapor is generated in the relatively lower part of the BF. While traveling with the gas stream to the upper part of the BF, Zn vapor is oxidized and condensed in the charged burdens or the refractory materials. As this sequence is repeated, ZnO is accumulated in the iron ore sinter and the refractory materials.[8,9] As ZnO content increases in the refractory material, damage of the refractory material may occur.[10] If we consider the maximum use of various dust (not only BF dust but also basic oxygen furnace dust[11,12] and electric arc furnace dust[13,14]), it is important to know the chemistry of iron ore sinter containing ZnO.

On the other hand, phases in the iron ore sinter are complex and mosaic structure is frequently observed. For the quantitative phase analysis of the iron ore sinter, the image analysis technique on the cross-sectional image has been generally applied[15,16] and the chemical composition of each phase has been determined using a scanning electron microscope-energy dispersive X-ray analyzer (SEM-EDX). However, the cross-sectional image does not provide adequate volume fractions of the phases so that an alternative technique for quantitative phase analysis should be considered. Hamilton

JUNWOO PARK, RAMARAGHAVULU RAJAVARAM, IN-KOOK SUH, and JOONHO LEE are with the Department of Materials Science and Engineering, Korea University, Seoul 02841, Republic of Korea. Contact email: joonholee@korea.ac.kr JIWON JEON and SANGHAN SON are with Technical Research Laboratories, POSCO, 6267, Donghaean-ro, Nam-gu, Pohang-si, Gyeongsangbuk-do, 37859, Republic of Korea.
Manuscript submitted March 24, 2020.
Article published online September 2, 2020.

et al. suggested that Rietveld analysis of the X-ray diffraction (XRD) patterns of the bulk sample would be the most promising method for the quantitative phase analysis,[17] and several researchers have adopted this method for the quantitative phase analysis.[18–24] For example, Webster *et al.* investigated the phase transition at high temperatures using *in-situ* synchrotron XRD.[18–23] More recently, Takayama *et al.* quantitatively analyzed the phases in iron ore sinters from sinter pot tests.[24]

Generally, iron ore sinter is composed of hematite, magnetite, silicoferrite of calcium and aluminum (SFCA), dicalcium silicate (C2S), *etc*. Since Hancart *et al.*[25] reported that SFCA was the major bonding phase in the iron ore sinter, many researchers[26–28] have explored the composition range of SFCA. Inoue and Ikeda[26] suggested a substitution plane of SFCA; the substitution plane, called the "CCC plane," was defined by the end members of $CaO \cdot 3Fe_2O_3$-$CaO \cdot 3Al_2O_3$-$CaO \cdot SiO_2$. Dawson *et al.*[27] reported the substitution plane as $CaO \cdot 2Fe_2O_3$-$CaO \cdot 2Al_2O_3$-$CaO \cdot 3SiO_2$. Patrick and Pownceby[28] suggested the substitution plane as $CaO \cdot 3$-Fe_2O_3-$CaO \cdot 3Al_2O_3$-$4CaO \cdot 3SiO_2$. Especially, calcium-ferrite–based materials are sensitive to several factors such as the composition,[29–36] thermal history,[37] and gas atmosphere.[18,38,39] Therefore, it is important to control the factors and analyze the samples exactly.

In the iron ore sinter, Zn may form zinc ferrite or can be dissolved in other phases. However, no study has been reported yet on the phase equilibria and solubility of Zn in other phases of the iron ore sinter. In this study, the form of Zn in the iron ore sinter is identified by using the Rietveld analysis of the XRD patterns of the iron ore sinters and SEM-EDX analysis of the phases. With varying the bulk sample composition, the effects of basicity and Al_2O_3 content on the chemistry of the phases in the iron ore sinter are investigated.

II. EXPERIMENTAL

In the present study, mostly reagent grade chemicals ($CaCO_3$, Fe_2O_3, SiO_2, Al_2O_3, and ZnO, 99 pct purity, < 100 μm) were used. $CaCO_3$ was calcined to obtain CaO at 1273 K (1000 °C) for 2 hours. CaO was then crushed and particles of 53 to 100 μm were used. Commercial grade coke, which was provided by POSCO, was used as a carbonaceous material. Coke particles, which were crushed and sieved to the same size as CaO, were selected and used in the present experiments. The chemicals at a predetermined ratio were mixed and pelletized in a drum mixer at 250 rpm for 2 hours, while distilled water was sprayed by 7 wt pct. Then, iron ore green pellets of 2 to 4 mm were selected and used for the lab-scale sintering simulation experiments. Table I shows the nominal composition of the sample pellets, and Table II summarizes the chemical composition of the coke used in this study. After experiments, the chemical composition of the sample was analyzed using inductively coupled plasma-atomic emission spectroscopy (ICP-AES) and wet-chemical analysis.

Figure 1 shows a schematic illustration of the experimental apparatus. An electric resistance furnace of a maximum temperature of 1573 K (1300 °C) was used. A vertical alumina reaction tube (ID: 60 mm, OD: 70 mm, and length: 1000 mm) was placed in the furnace, and both sides of the tube were sealed with stainless cooling jackets. An alumina tube (ID: 47 mm, OD: 54 mm, and length: 314 mm) was attached to the bottom jacket with O-rings and another alumina tube (length: 100 mm) was placed above it. Between the two alumina tubes, a

Table II. Composition of Coke Used in the Present Study (Weight Percent)

Composition of the Coke			
Moisture	Volatile Matter	Ash	Fixed Carbon
0.22	1.76	11.66	86.36

Composition of Ash in the Coke				
Fe_2O_3	FeO	SiO_2	CaO	MgO
6.08	< 0.1	54.55	2.78	0.87

Composition of Ash in the Coke				
Al_2O_3	ZnO	P_2O_5	Na_2O	K_2O
27.40	0.03	1.09	0.44	1.28

Table I. Nominal Composition of the Samples before Experiments (Weight Percent)

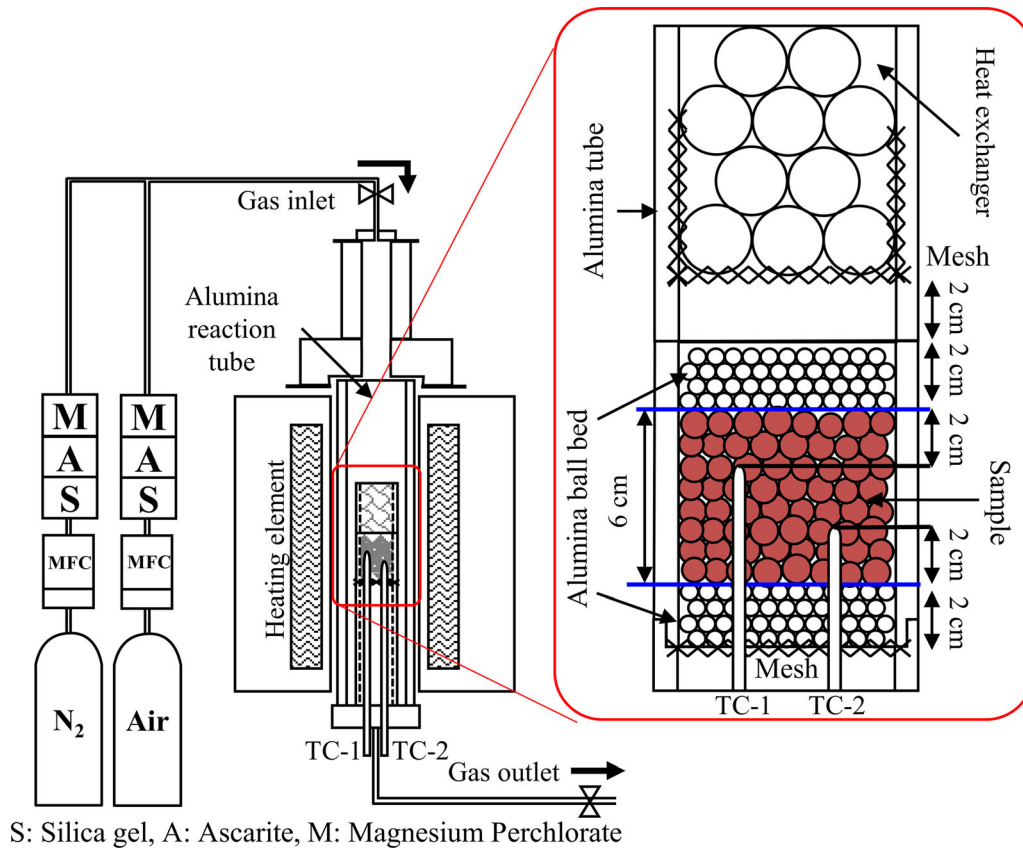| Sample	Fe_2O_3	CaO	SiO_2	Al_2O_3	ZnO	Coke	Basicity (CaO/SiO_2)
1	75.5	13.4	6.6	1	1	2.5	2
2	74.5	13.4	6.6	1	2	2.5	2
3	73.5	13.4	6.6	1	3	2.5	2
4	75.5	15.0	5.0	1	1	2.5	3
5	75.5	16.0	4.0	1	1	2.5	4
6	74.5	13.4	6.6	2	1	2.5	2
7	73.5	13.4	6.6	3	1	2.5	2

Fig. 1—Schematic diagram of the sintering simulator.

stainless-steel mesh was placed to support the sample particles. At the bottom, alumina balls of 2 mm in diameter were charged to the height of 20 mm to prevent the dropping of molten phases during experiments. Then, pellets were charged in a 60-mm-thick layer. Finally, alumina balls of 2 mm in diameter were added on the top in a 20-mm thickness. Twenty millimeters above the sample particles, a heat exchanger composed of alumina balls of 10 mm in diameter was placed to prevent the chilling of the sample particles by rapid gas flows. To monitor temperature variation during experiments, two type-R thermocouples were buried in the sample pellets: one (TC-1) at a position 20 mm below from the top surface of the pellet layer and the other (TC-2) 20 mm below from TC-1.

Once the sample assembly was installed, it was heated to 1273 K (1000 °C) at a heating rate of $+10$ K/min ($+10$ °C/min) while flowing N_2 gas from the top of the reaction tube at a flowing rate of 300 mL/min STP. At 1273 K (1000 °C), 79 pct N_2-21 pct O_2 gas mixture was injected at a flowing rate of 20 L/min STP. Owing to the rapid chemical reaction between coke particles and oxygen, the temperature of the sample instantaneously increased. Figure 2 shows a typical result of the temperature variation of the sample. In 60 seconds, temperature monitored with TC-1 reaches a maximum temperature of 1573 K (1300 °C) and then decreases monotonically. Temperature monitored with TC-2 shows a similar variation with a time interval of 40
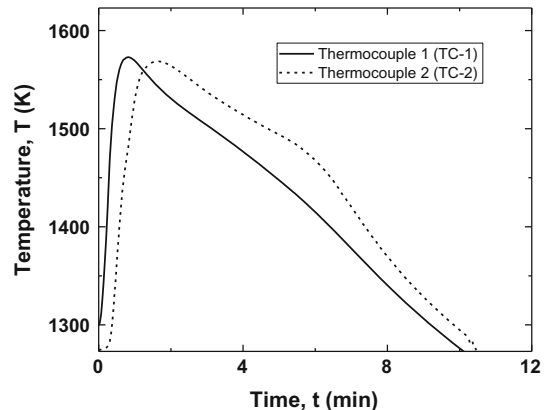

Fig. 2—Typical temperature profiles of the sample, which were measured with TC-1 and TC-2.

seconds. From the difference in temperature variations monitored with two thermocouples, the moving velocity of the combustion zone was estimated to be approximately 0.5 mm/s. When the temperature of TC-1 decreased to 1273 K (1000 °C), the electric current applied to the furnace was shut down and the sample was cooled to room temperature in the furnace. Due to the temperature profile obtained in this experimental
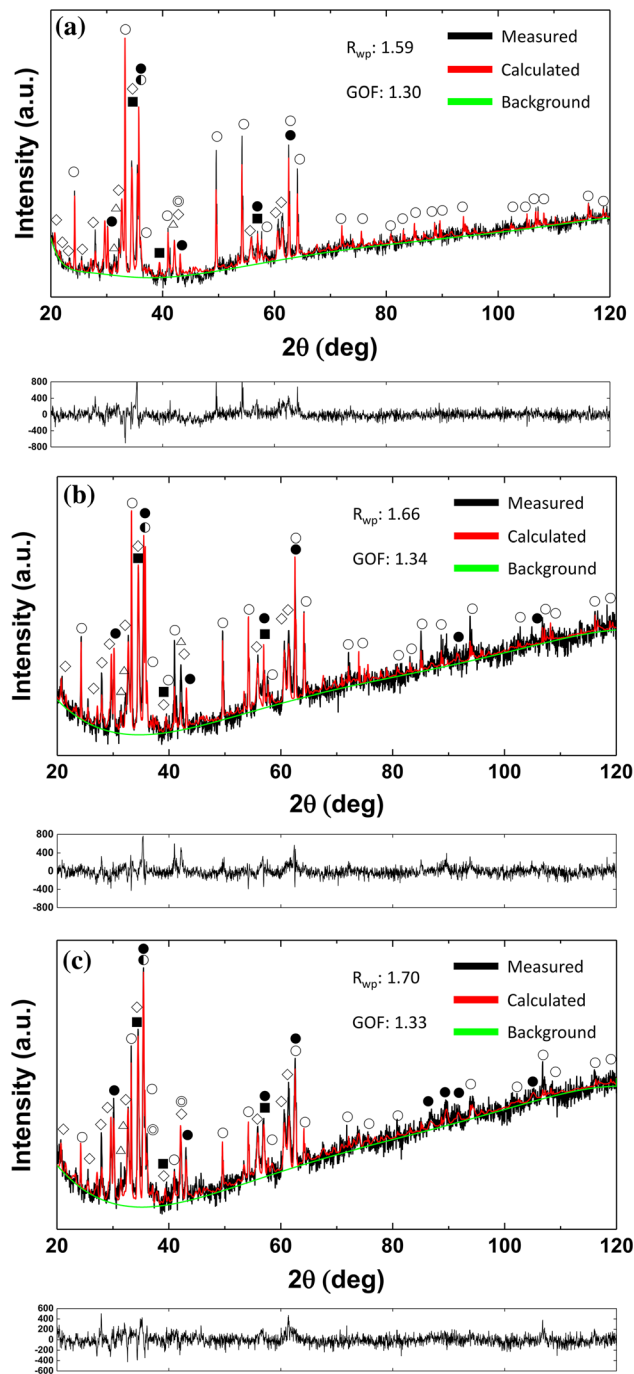
Fig. 3—XRD patterns and Rietveld analysis results of the sinter samples: (*a*) sample 1, (*b*) sample 2, and (*c*) sample 3. ○: Fe_2O_3, ●: Fe_3O_4, ◇: SFCA, △: C2S, ◎: FeO, ◐: franklinite, and ■: Al_2O_3. At the bottom of each figure, differences between the calculated and measured profiles are shown.

setup, it was possible to demonstrate the initial stage of the practical sinter process with this experimental facility.

After the experiments, XRD analysis (D8 Advance, Bruker, Cu K_α target, 40 kV, 40 mA), wet-chemical analysis, and SEM-EDX analysis were carried out to identify the phases and compositions of the samples. In XRD analysis, the 2θ range was varied from 20 to 120

deg at the scan speed of 0.8 deg/min. X'Pert HighScore Plus 4.7(Malvern Panalytical, Netherlands) was used to refine the phases and to perform Rietveld analysis.

III. RESULTS AND DISCUSSION

A. *Effect of ZnO*

To investigate the behavior of Zn in the iron ore sinters, ZnO content in the raw mixtures was varied from 1 to 3 wt pct (samples 1 through 3), while the basicity was fixed at 2 and the Al_2O_3 content was 1 wt pct. Figure 3 shows the identification results of XRD patterns of samples 1 through 3, and the comparison between the calculated and measured XRD patterns. At the bottom of each figure, differences between the calculated and measured profiles are shown. Commonly, Fe_2O_3, Fe_3O_4, FeO, SFCA, C2S, franklinite, and Al_2O_3 were identified. No zincite (ZnO) was detected in the present samples. Since the binary system of franklinite and Fe_3O_4 is isomorphous, the XRD patterns for franklinite and Fe_3O_4 are almost identical. Therefore, the phase ratio was calculated with the values of lattice parameters of franklinite and Fe_3O_4.[40] In XRD patterns, various calcium ferrite phases, such as $CaFe_2O_4$ (CF),[41] $Ca_2Fe_2O_5$ (C2F),[42] and $CaFe_4O_7$ (CF2),[43] were also detected, but the amount of each phase was less than 0.6 wt pct. Therefore, these phases were excluded from the quantitative analysis. The formation behavior of complex calcium ferrites depends on oxygen partial pressure.[18,38] Among various complex calcium ferrites, SFCA was the main mineral phase. It is considered that high oxygen partial pressure leads to a favorable condition for forming the SFCA. SFCA was generated by the reaction between the liquid phase and magnetite during sintering, as suggested by Webster *et al.*[19] The Rietveld analysis results are summarized in Table III, and the phase fractions are shown as a function of bulk ZnO content in Figure 4. In this study, the weighted profile R factor (R_{wp}) and goodness-of-fit values on the Rietveld analysis are within the acceptable ranges of 1.59 to 1.97 and 1.30 to 1.55, respectively. With increasing ZnO content, the phase fractions of SFCA, Fe_3O_4, C2S, FeO, and franklinite increased, whereas that of Fe_2O_3 decreased. Chemical analysis results are summarized in Table IV. It can be expected that some amount of ZnO could be reduced by coke during the experiments, but no significant change in ZnO content was noticed in this study. Besides, from the XRD analysis, zincite was not detected. Accordingly, it was considered that ZnO was dissolved in some phases such as franklinite.

To identify each mineral phase, the cross-sectional images were taken by using backscattered electron (BSE) microscopy. Then, SEM-EDX analysis was carried out to investigate the chemical composition of the selected phases. Figure 5 shows the BSE micrographs for samples 1 through 3. It is found

Table III.

Table III. Phase Fractions of Mineral Phases in the Samples Determined by Rietveld analysis (Weight Percent)

| | | | Phase Fractions | | | | |
| | | | | Spinel | | | |
Sample	SFCA	Fe_2O_3	Fe_3O_4	Franklinite	C2S	FeO	Al_2O_3
1	47.4	29.9	7.2	1.1	9.1	3.7	1.6
2	50.1	19.8	9.5	3.2	10.1	5.6	1.6
3	53.1	13.5	10.9	4.5	10.2	6.5	1.4
4	67.8	8.6	3.1	0.4	8.7	8.3	3.2
5	79.2	2.2	1.5	0.2	9.1	6.3	1.5
6	61.2	20.4	7.2	0.4	4.9	4.6	1.3
7	83.2	6.3	3.6	0.2	2.1	3.2	1.4
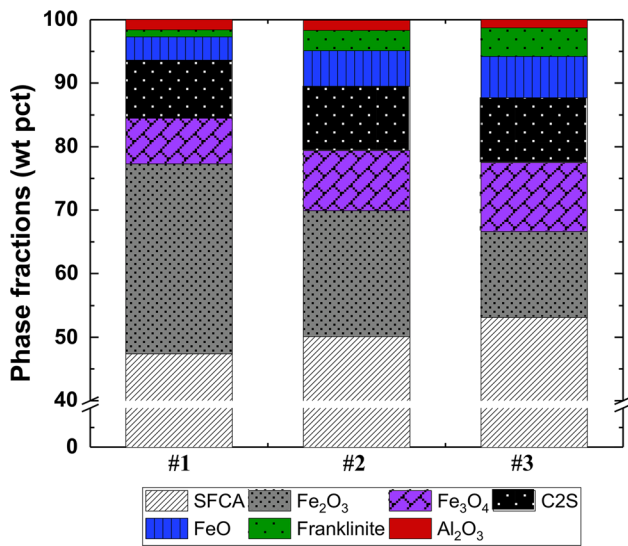
Fig. 4—Phase fractions in the sinter with respect to ZnO content, while the basicity was fixed at 2 and the Al_2O_3 content was 1 wt pct: (1) 1 wt pct ZnO, (2) 2 wt pct ZnO, and (3) 3 wt pct ZnO.

Table IV. Chemical Compositions of the Samples by ICP and Wet-Chemical Analysis (Weight Percent)

| | Chemical Composition | | | | | | |
Sample	Fe_2O_3	FeO	M·Fe	CaO	SiO_2	Al_2O_3	ZnO
1	71.97	5.32	0.39	13.00	6.22	2.20	0.90
2	71.97	4.45	0.47	12.85	6.00	2.40	1.87
3	70.34	5.34	0.49	13.08	5.58	2.38	2.79
4	71.62	4.48	0.40	13.99	4.54	4.01	0.96
5	71.39	5.35	0.41	15.59	3.88	2.48	0.90
6	71.11	5.34	0.43	12.75	5.88	3.58	0.90
7	69.44	4.73	0.46	12.83	5.86	5.74	0.95

that needlelike SFCA, Fe_2O_3, and Fe_3O_4 are the dominant phases. FeO, franklinite, and Al_2O_3 were detected from XRD analysis but are too small to be investigated from the cross-sectional image. From
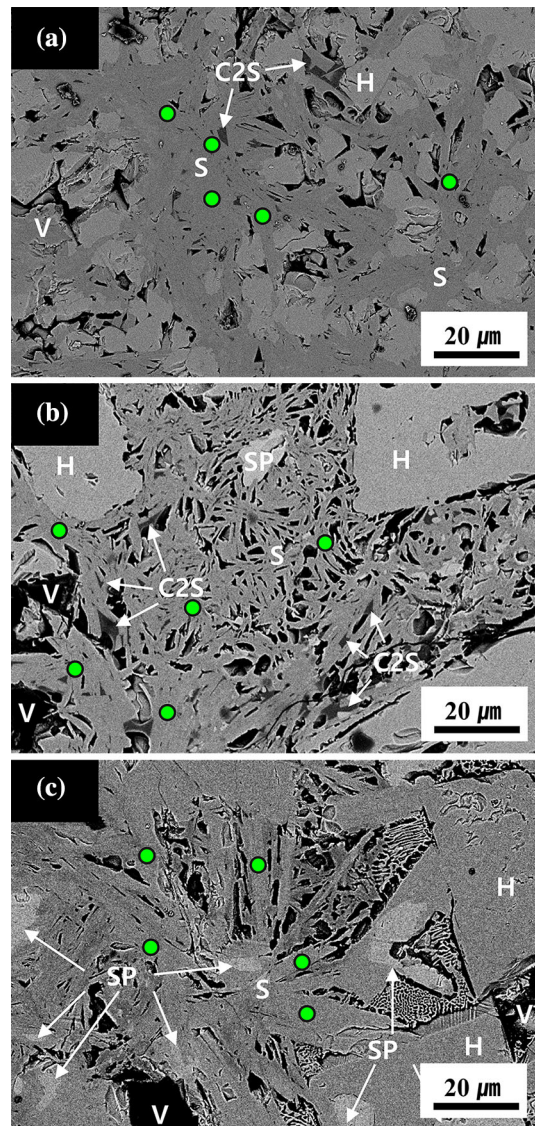

Fig. 5—BSE micrograph of the samples: (a) sample 1 (1 wt pct ZnO), (b) sample 2 (2 wt pct ZnO), and (c) sample 3 (3 wt pct ZnO). S: SFCA, H: hematite, SP: spinel group including magnetite and franklinite, C2S: dicalcium silicate, V: void, and EDX analysis points are indicated as green dots (Color figure online).

Table V.   Composition of SFCA Analyzed with EDX: Average Value of Three Points (Weight Percent)

Sample	Fe_2O_3	CaO	SiO_2	Al_2O_3	ZnO
1	80.46 ($\pm$ 1.91)	11.13 ($\pm$ 1.55)	5.76 ($\pm$ 0.82)	1.30 ($\pm$ 0.43)	1.34 ($\pm$ 0.24)
2	78.33 ($\pm$ 2.82)	12.76 ($\pm$ 1.57)	5.51 ($\pm$ 0.64)	1.75 ($\pm$ 0.48)	1.66 ($\pm$ 0.39)
3	79.37 ($\pm$ 1.23)	11.98 ($\pm$ 1.19)	4.93 ($\pm$ 1.02)	1.88 ($\pm$ 0.88)	2.02 ($\pm$ 0.39)
4	85.83 ($\pm$ 1.86)	9.30 ($\pm$ 1.02)	2.39 ($\pm$ 0.64)	1.01 ($\pm$ 0.37)	1.48 ($\pm$ 0.31)
5	85.94 ($\pm$ 1.11)	10.26 ($\pm$ 0.25)	1.57 ($\pm$ 0.75)	1.15 ($\pm$ 0.40)	1.08 ($\pm$ 0.34)
6	75.02 ($\pm$ 2.40)	14.28 ($\pm$ 1.30)	6.08 ($\pm$ 1.69)	3.57 ($\pm$ 0.79)	1.06 ($\pm$ 0.22)
7	71.85 ($\pm$ 1.91)	14.85 ($\pm$ 1.15)	6.69 ($\pm$ 0.78)	5.29 ($\pm$ 0.64)	1.33 ($\pm$ 0.38)

EDX analysis, Zn was detected in SFCA. To obtain the average composition of SFCA, three points of SFCA for each sample were investigated with SEM-EDX. The analyzed points are indicated as green dots in Figure 4. The average composition of SFCA is summarized in Table V. It is found that SFCA contained 1.34 to 2.02 wt pct ZnO. Accordingly, the majority of the increased ZnO resulted in the formation of the franklinite. Since Zn has low boiling temperature and high vapor pressure, it can be easily volatilized during the sinter plant operation under a reducing atmosphere.[6] However, from this study, it was confirmed that ZnO formed franklinite and it was partially dissolved in SFCA at least in the initial stage of the practical sinter operation. It should be noted that the reducing condition was maintained only for 60 seconds, while coke particles reacted with the 79 pct N_2 to 21 pct O_2 carrier gas mixture, and after consuming coke particles, it was switched to the oxidizing condition. In a conventional sinter plant, reduction and evaporation of Zn and reoxidation may occur simultaneously.[12] To investigate the removal of Zn in a conventional sinter plant, kinetic studies should be carried out separately under isothermal conditions for a longer period.

B. Effect of Basicity

To investigate the effect of basicity, the basicity was controlled from 2 to 4, while the ZnO and Al_2O_3 contents were fixed at 1 wt pct, respectively. For this purpose, samples 1, 4, and 5 are compared. Figure 6 shows the identification results of the XRD patterns of samples 4 and 5. Fe_2O_3, Fe_3O_4, FeO, SFCA, C2S, franklinite, and Al_2O_3 were identified for these samples. The Rietveld analysis results are summarized in Table III and graphically shown in Figure 7. The amount of SFCA increased with increasing basicity, whereas those of Fe_2O_3, Fe_3O_4, and franklinite decreased.

Figure 8 shows the BSE microscope observation results of samples 4 and 5. It is found that with increasing basicity, the fraction of SFCA increased from 47.4 to 79.2 wt pct and the width of the columnar SFCA became larger. As the fraction of SFCA increased, the fraction of franklinite decreased from 1.1 to 0.2 wt pct, while ZnO content in the SFCA was almost constant in the range of 1.08 to 1.48 wt pct (Table V). Accordingly,
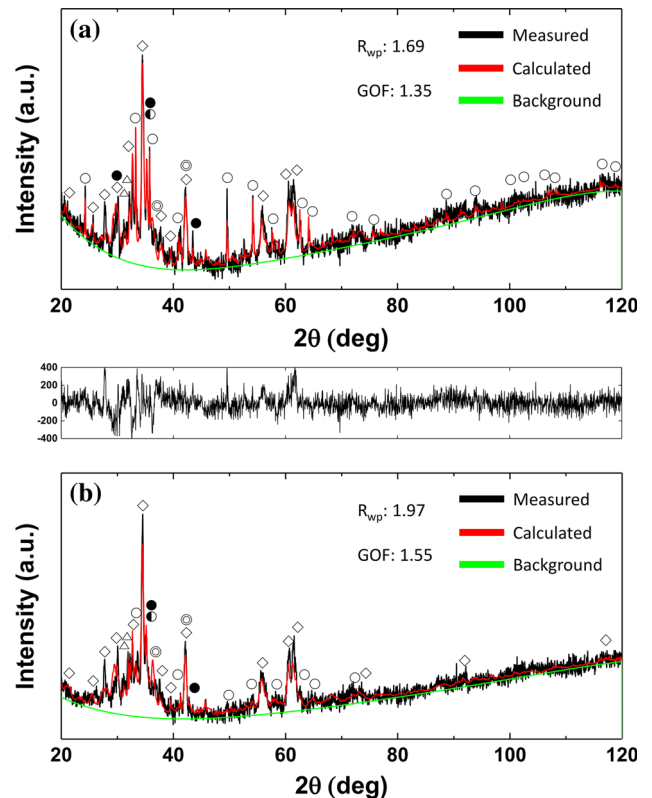

Fig. 6—XRD patterns and Rietveld analysis results of sinter samples: (a) sample 4 and (b) sample 5. ○: Fe_2O_3, ●: Fe_3O_4, ◇: SFCA, △: C2S, ◎: FeO, ◖: franklinite, and ■: Al_2O_3. At the bottom of each figure, differences between the calculated and measured profiles are shown.

it is considered that as the basicity increased, ZnO tended to be preferentially dissolved in SFCA rather than forming franklinite.

C. Effect of Al_2O_3

To investigate the effect of Al_2O_3, the Al_2O_3 content in the iron ore sinter was controlled from 1 to 3 wt pct, while the basicity was fixed at 2 and the ZnO content was 1 wt pct. For this purpose, samples 1, 6, and 7 are
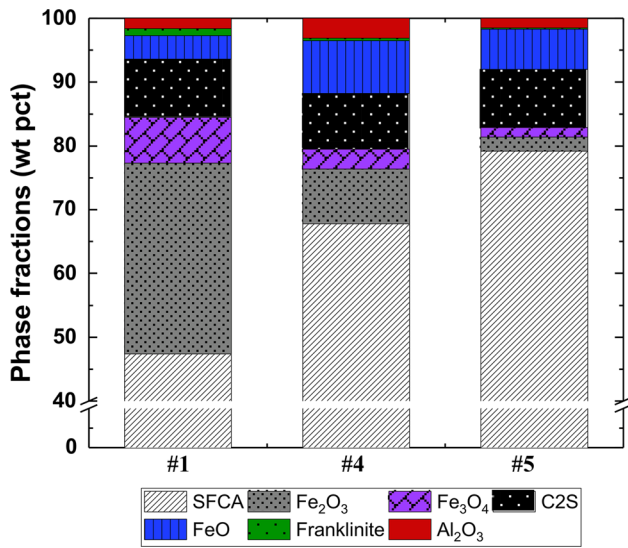
Fig. 7—Phase fractions in the sinter with respect to basicity, while the ZnO and Al$_2$O$_3$ contents were fixed at 1 wt pct, respectively.

Fig. 8—BSE micrograph of the samples: (*a*) sample 4 (basicity 3) and (*b*) sample 5 (basicity 4). S: SFCA, C2S: dicalcium silicate, A: Al$_2$O$_3$, V: void, and EDX analysis points are indicated as green dots (Color figure online).

compared. Figure 9 shows the identification results of the XRD patterns of samples 6 and 7, and the Rietveld analysis results are graphically shown in Figure 10. As the Al$_2$O$_3$ content increased from 1 to 3 wt pct, the amount of SFCA increased from 47.4 to 83.2 wt pct. On the other hand, the amount of Fe$_2$O$_3$, Fe$_3$O$_4$, and franklinite decreased. Al$_2$O$_3$ is known as a stabilizing element for the formation of calcium ferrite,[44–46] and Webster *et al*.[19] reported that with increasing Al$_2$O$_3$ content, the formation temperature of SFCA in the cooling process increased. Accordingly, increased Al$_2$O$_3$ content would accelerate the formation of SFCA in the sinter.

Figure 11 shows the BSE microscope observation results of samples 6 and 7. There is no significant morphological change investigated in these samples. The ZnO content in SFCA of each sample did not change so much with increasing the Al$_2$O$_3$ content, while the fraction of SFCA considerably increased. Accordingly, it is concluded that most of the ZnO is dissolved in the SFCA phase.

D. Crystal Structure Change of SFCA

In the crystal structure of SFCA, the substitution of atoms is performed between tetragonal sites and octahedral sites. Hamilton *et al*.[17] reported that substitutions are made in M6, Ca1, and M12 sites. Here, M6 and M12 are the tetrahedral sites and Ca1 is the octahedral site. Figure 12 shows the positions of the atoms in the crystal structure. They assumed that M6 is occupied by Al, while M12 is substituted between Si and Al, and Ca1 is substituted between Ca and Fe. In this study, for the first time, it can be assumed that Zn substitutes the tetragonal sites as well as the octahedral sites. The probable position of the Zn atom is then simulated by placing the Zn atom in each site using a simulation program, X'pert highs score. The simulation
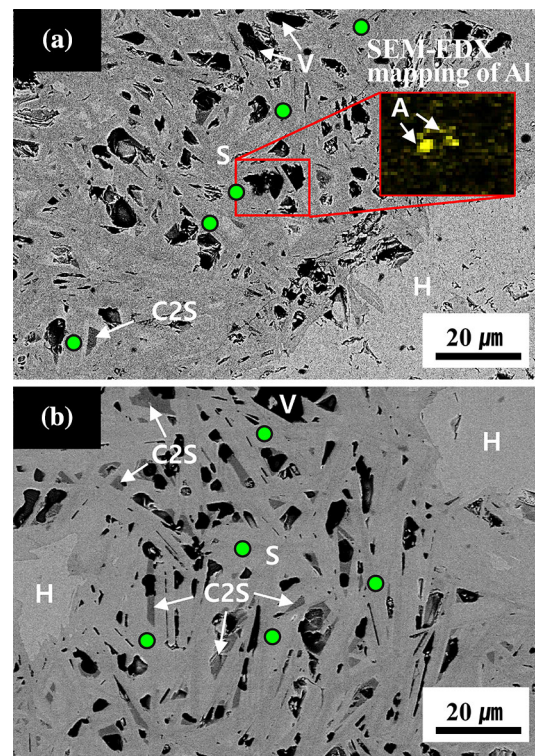
results are summarized in Table VI. The atomic coordinate information of the substitution site, which is used in the simulation and reported by Hamilton et al.,[17] is indicated in Table VII. The simulation results show that the most probable position of Zn is the M12 sites. Takayama *et al*.[24] reported that Fe can be substituted not only at Ca1 sites but also at M6 sites. In this study, to satisfy the mass balance of Fe in SFCA, it was optimized that Fe substituted at all M6, Ca1, and M12 sites.

Figure 13 shows the composition change in SFCA obtained from EDX analysis and the change of the atomic occupancy at M6, Ca1, and M12 sites as ZnO content in sinter increases. As the initial ZnO content increases, the concentrations of ZnO and Al$_2$O$_3$ in SFCA increase, whereas that of SiO$_2$ decreases. Structural analysis reveals that Fe mostly occupies M6 and Ca1 sites. On the other hand, Si, Zn, and Al occupy M12 sites, where the substitution occurs. With increasing ZnO content, Zn and Al occupancies increase, whereas Si occupancy decreases.

Figure 14 shows the composition change in SFCA and the change of the atomic occupancy at M6, Ca1, and M12 sites as basicity in sinter increases. As the basicity increases, the concentration of Fe$_2$O$_3$ increases, while that of SiO$_2$ decreases. This trend is also related to the increased occupancy of Fe at the M12 sites and the decreased occupancy of Si. However, there is no significant change in the Zn occupation at the M12 sites.
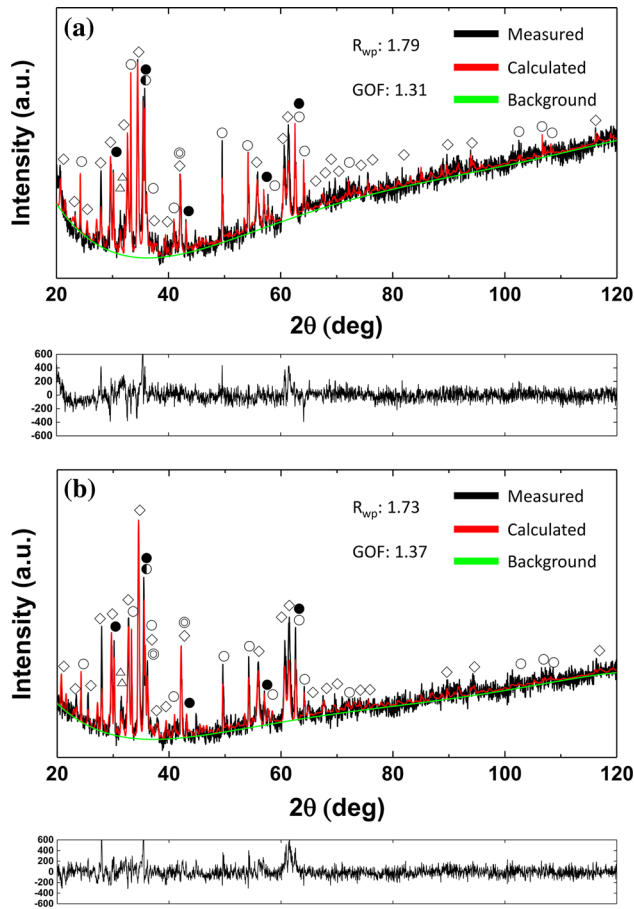
Fig. 9—XRD patterns and Rietveld analysis results of sinter samples: (a) sample 6 and (b) sample 7. ○: Fe_2O_3, ●: Fe_3O_4, ◇: SFCA, △: C2S, ◎: FeO, ◐: franklinite, and ■: Al_2O_3. At the bottom of each figure, differences between the calculated and measured profiles are shown.
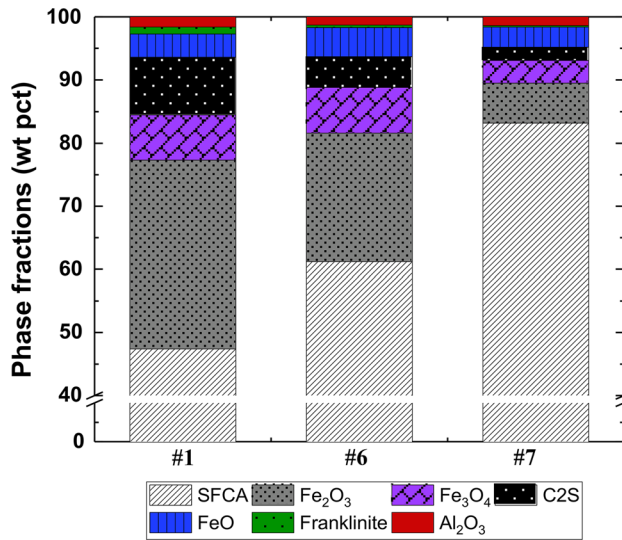

Fig. 10—Phase fractions in the sinter with respect to the Al_2O_3 content, while the basicity was fixed at 2 and the ZnO content was 1 wt pct.
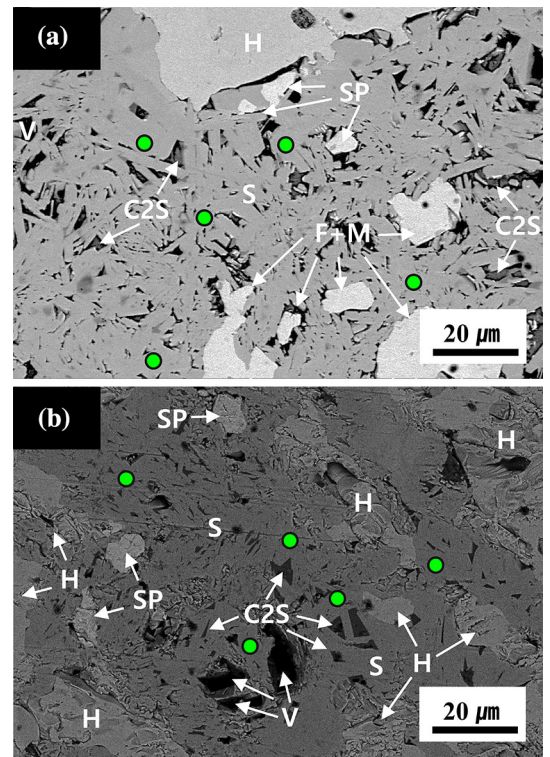

Fig. 11—BSE micrograph of the samples: (a) sample 6 (2 wt pct Al_2O_3) and (b) sample 7 (3 wt pct Al_2O_3). S: SFCA, H: hematite, SP: spinel group including magnetite and franklinite, C2S: dicalcium silicate, V: void, and EDX analysis points are indicated as green dots (Color figure online).
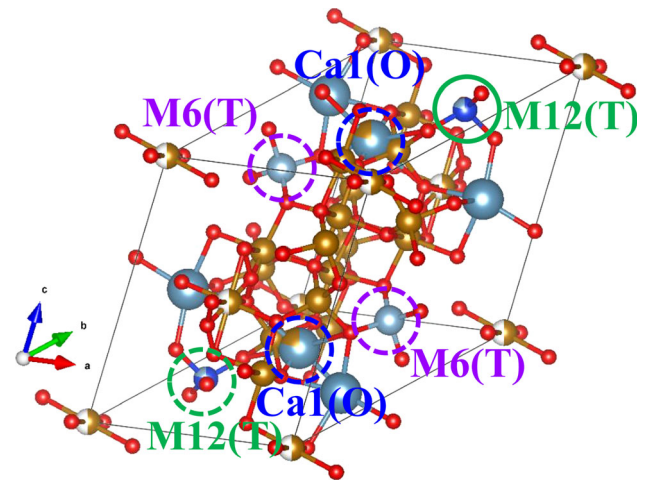
Fig. 12—Crystal structure of SFCA($Ca_{2.8}Fe_{8.7}Al_{1.2}Si_{0.8}O_{20}$); T: tetrahedral site and O: octahedral site.

Figure 15 shows the composition change in SFCA and the change of the atomic occupancy at M6, Ca1, and M12 sites as Al_2O_3 content in sinter increases. As the initial Al_2O_3 content increases from 1 to 3 wt pct, the concentration of Al_2O_3 in the SFCA increases from 1.30 to 5.29 wt pct, whereas that of Fe_2O_3 decreases from 80.46 to 71.85 wt pct. This trend is related to the increased occupancy of Al and the decreased occupancy

Table VI. Crystal Structural Analysis Results of SFCA Containing ZnO

Atom Site	Atom		Probable Occupancy						
	Ref. [17]	This Study	1	2	3	4	5	6	7
M6	Al	Al/Fe	0/1	0/1	0/1	0/1	0/1	0.1/0.9	0.4/0.6
Ca1	Ca/Fe	Ca/Fe	0/1	0/1	0/1	0/1	0/1	0.6/0.4	0.2/0.8
M12	Si/Al	Si/Al / Zn/Fe	0.7/0.1 /0.2/0	0.6/0.15 /0.25/0	0.45/0.2 /0.35/0	0.2/0.1 /0.2/0.5	0.1/0.1 /0.2/0.6	0.6/0.2 /0.2/0	0.7/0.1 /0.2/0

Table VII. Atomic Coordinates of M6, Ca1, and M1 in SFCA[17]

Atom Site	Atomic Coordinates (nm)		
	x	y	z
M6	0.8374	0.5293	0.2345
Ca1	0.5558	0.404	0.1563
M12	0.7282	0.7307	0.9286

of Fe in the M6 sites. However, it is noticeable that atomic occupancy at the M12 sites does not change considerably. The atomic occupancy at the Ca1 sites is relatively complex. Nevertheless, the occupancy of Zn is investigated at the M12 sites only, and it did not change with increasing Al_2O_3 content.

Based on the preceding simulation results, it is concluded that when ZnO is added in the sinter, it is dissolved in the SFCA phase and Zn preferentially occupies the M12 site. It is also found that the basicity and content of Al_2O_3 do not affect the dissolution behavior of Zn in the SFCA phase. Since the Rietveld
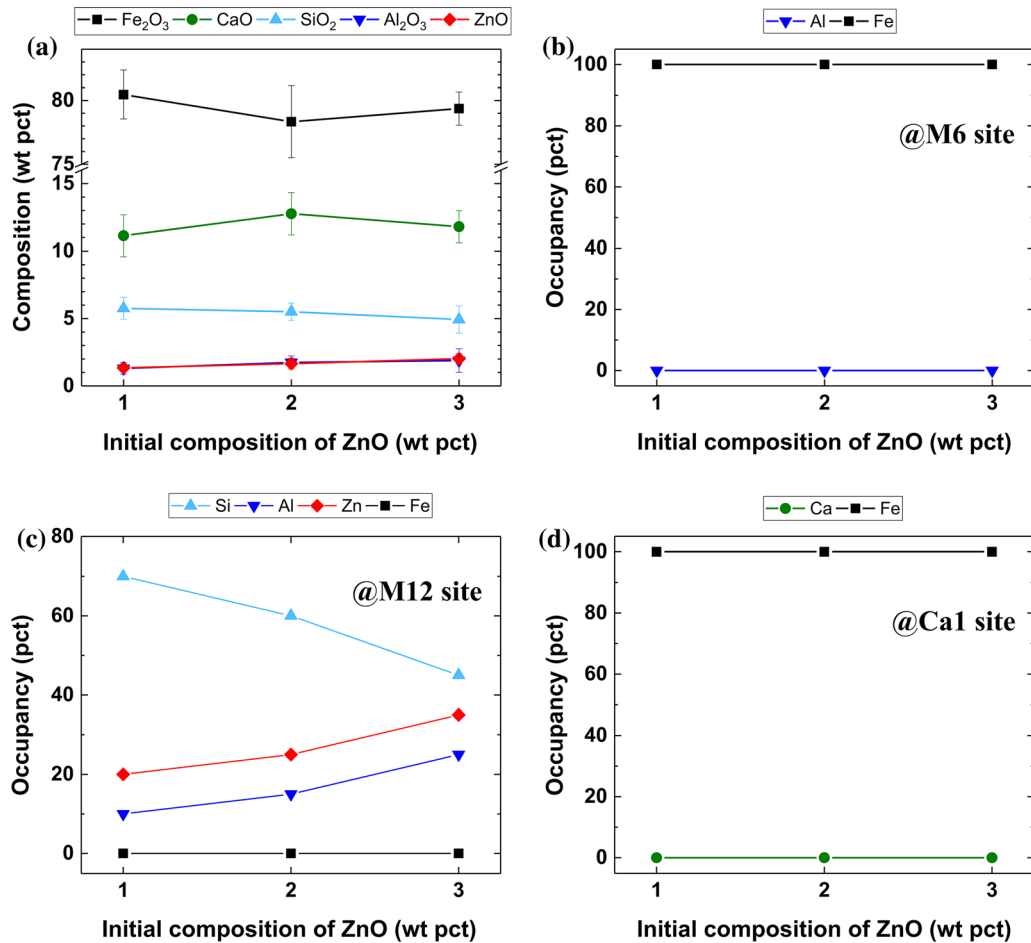

Fig. 13—Composition change in SFCA and atom occupancy change in SFCA with respect to the ZnO content: (a) composition of SFCA from EDX, (b) atom occupancy changes in the M6 site, (c) atom occupancy changes in the M12 site, and (d) atom occupancy changes in the Ca1 site.
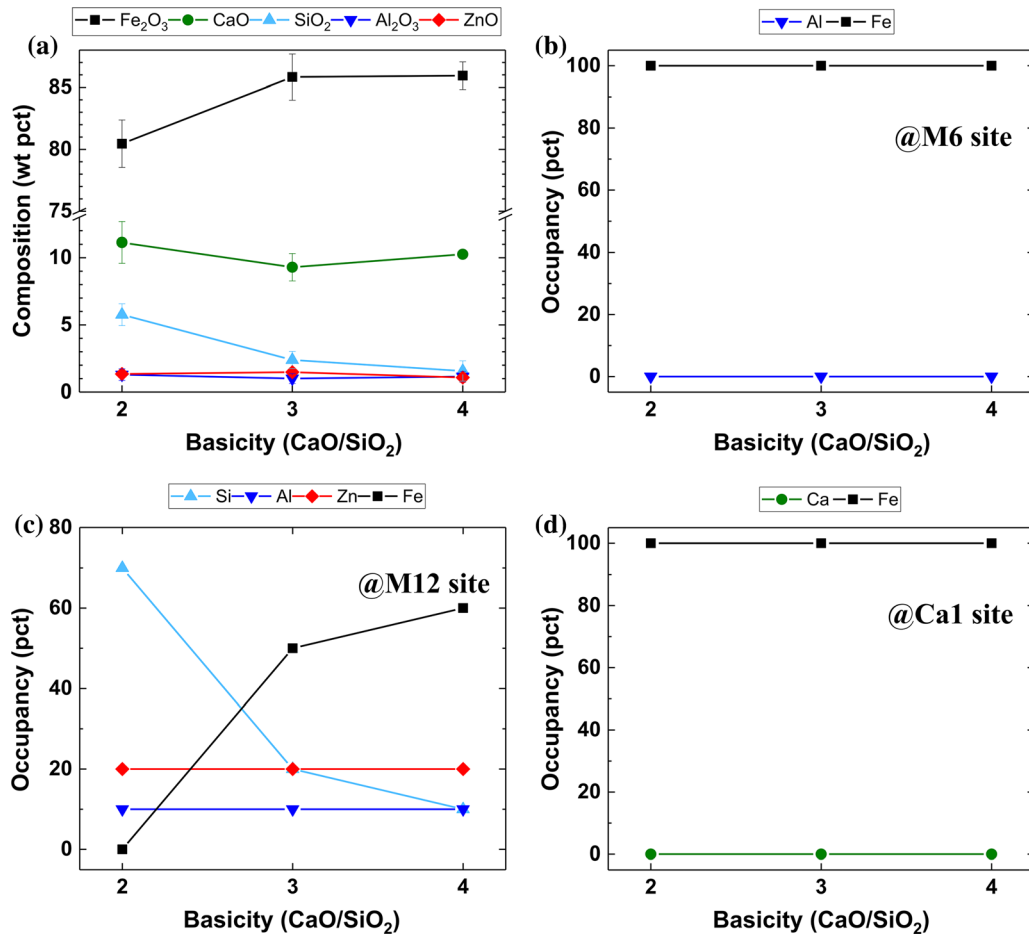
Fig. 14—Composition change in SFCA and atom occupancy change in SFCA with respect to basicity: (*a*) composition of SFCA from EDX, (*b*) atom occupancy changes in the M6 site, (*c*) atom occupancy changes in the M12 site, and (*d*) atom occupancy changes in the Ca1 site.

analysis results are comparable with the SEM-EDX analysis results, it is quite reasonable to accept the simulation results.

IV. CONCLUSIONS

As the use of by-products increases in the iron ore sinter process, it is necessary to understand the phase stability of the iron ore sinter containing ZnO. In this study, the effects of the ZnO addition, basicity, and Al_2O_3 content on the behavior of Zn in the iron ore sinter were investigated. The phase fractions, the composition of SFCA, and the substitution sites of Zn could be identified by using Rietveld analysis, wet-chemical

analysis, and SEM-EDX analysis. It was confirmed that ZnO existed as franklinite or was dissolved in the SFCA phase of the iron ore sinter. As the ZnO content increased, the amount of franklinite and SFCA increased, while the amount of Fe_2O_3 decreased. It was considered that Zn occupies the M12 sites of the SFCA phase. As the basicity of the iron ore sinter increased, the amount of franklinite considerably decreased, while the amount of SFCA increased. Here, the occupancy rate of Zn in the M12 sites did not change so much in the SFCA phase. As the Al_2O_3 content increased, the amount of franklinite slightly decreased and the amount of SFCA remarkably increased. Here, the occupancy rate of Zn in the M12 sites remained almost constant. Accordingly, with increasing Al_2O_3,
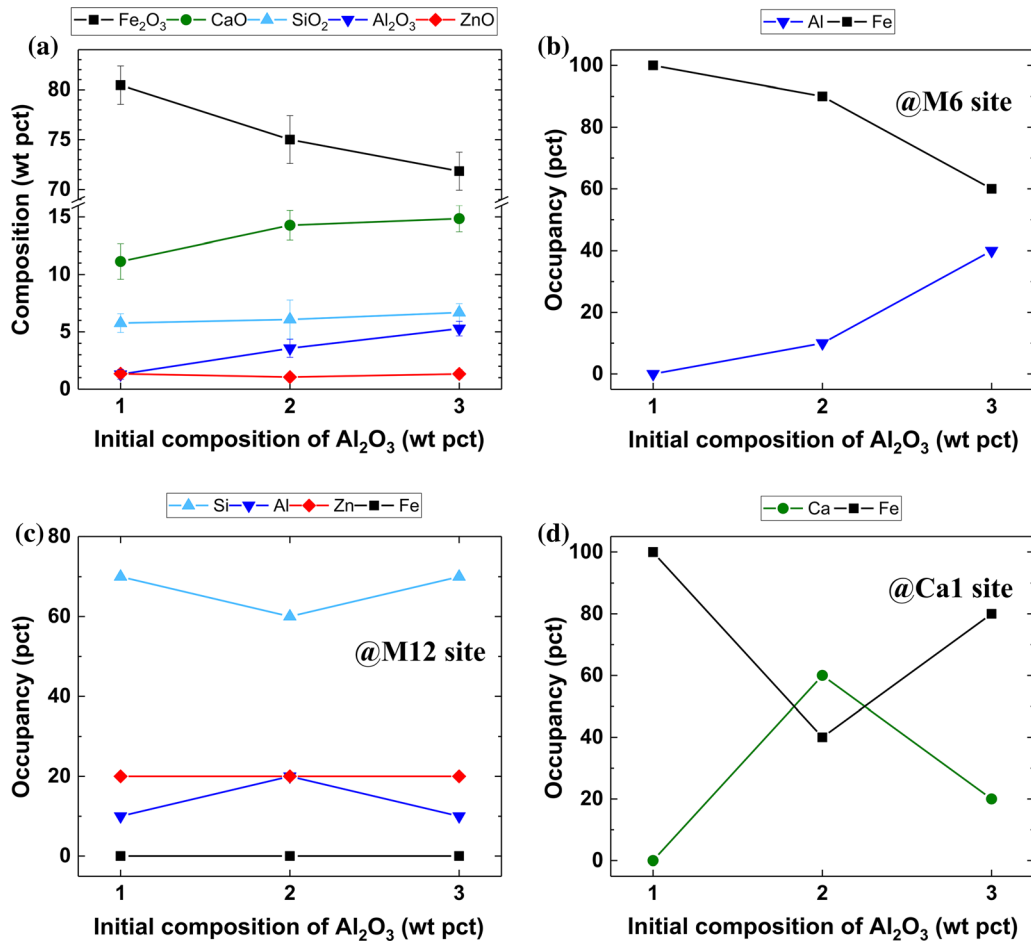
Fig. 15—Composition change in SFCA and atom occupancy change in SFCA with respect to Al_2O_3 content: (*a*) composition of SFCA from EDX, (*b*) atom occupancy changes in the M6 site, (*c*) atom occupancy changes in the M12 site, and (*d*) atom occupancy changes in the Ca1 site.

the SFCA containing ZnO became more stable. From this study, it is concluded that to remove Zn from the iron ore sinter, a kinetic study on the chemical reaction between CO and Zn in the SFCA is required in the future.

REFERENCES

1. H.T. Makkonen, J. Heino, L. Laitila, A. Hiltunen, E. Poylio, and J. Harkki: *Resour. Conserv. Recycle*, 2002, vol. 35, pp. 77–84.
2. D. Hleis, I. Fernandez-Olmo, F. Ledoux, A. Kfoury, L. Courcot, T. Desmonts, and D. Courcot: *J. Hazard. Mater.*, 2013, vols. 250–251, pp. 246–55.
3. N.C.C. Lobato, E.A. Villegas, and M.B. Mansur: *Resour. Conserv. Recycle*, 2015, vol. 102, pp. 49–57.
4. C. Lanzerstorfer: *ISIJ Int.*, 2017, vol. 57, pp. 1484–89.

5. B. Asadi Zeydabadi, D. Mowla, M.H. Shariat, and J. Fathi Kalajahi: *Hydrometallurgy*, 1997, vol. 47, pp. 113–25.
6. C. Lanzerstorfer, B. Bamberger-Strassmayr, and K. Pilz: *ISIJ Int.*, 2015, vol. 55, pp. 758–64.
7. W. Lv, M. Gan, X. Fan, Z. Ji, X. Chen, J. Yao, and T. Jiang: *JOM*, 2019, vol. 71, pp. 3173–80.
8. D.E. Esezobor and S.A. Balogun: *Ironmak. Steelmak.*, 2006, vol. 33, pp. 419–25.
9. P. Besta, K. Janovska, A. Samolejova, A. Berankova, I. Voznakova, and M. Hendrych: *Metalurgija*, 2013, vol. 52, pp. 197–200.
10. K. Narita, T. Onoye, Y. Satoh, M. Miyamoto, K. Taniguchi, S. Kamatani, T. Sato, and S. Fukihara: *Trans. ISIJ*, 1981, vol. 21, pp. 839–45.
11. J. Wang, Z. Wang, Z. Zhang, and G. Zhang: *Metall. Mater. Trans. B*, 2019, vol. 50B, pp. 480–90.
12. H. Li, D.J. Pinson, P. Zulli, L. Lu, R.J. Longbottom, S.J. Chew, B.J. Monaghan, and G. Zhanga: *J. Hazard. Mater.*, 2020, vol. 385, p. 121592.
13. H. Ishikawa, J. Kopfle, J. McClelland, and J. Ripke: *Arch. Metall. Mater.*, 2008, vol. 53 (2), pp. 541–45.
14. R.A. Shawabkeh: *Hydrometallurgy*, 2010, vol. 104, pp. 61–65.
15. A. Greco, D. Jeulin, and J. Serra: *J. Microsc.*, 1979, vol. 116, pp. 199–211.
16. Z. Wang, D. Pinson, S. Chew, B.J. Monaghan, M.I. Pownceby, N.A.S. Webster, H. Rogers, and G. Zhang: *ISIJ Int.*, 2016, vol. 56, pp. 1138–47.
17. J.D.G. Hamilton, B.F. Hoskins, W.G. Mumme, W.E. Borbidge, and M.A. Montague: *Neues Jahrb. Mineral. Abh.*, 1989, vol. 161, pp. 1–26.
18. N.A.S. Webster, M.I. Pownceby, I.C. Madsen, and J.A. Kimpton: *ISIJ Int.*, 2013, vol. 53, pp. 774–81.
19. N.A.S. Webster, M.I. Pownceby, I.C. Madsen, and J.A. Kimpton: *Metall. Mater. Trans. B*, 2012, vol. 43B, pp. 1344–57.
20. N.A.S. Webster, M.I. Pownceby, and I.C. Madsen: *ISIJ Int.*, 2013, vol. 53, pp. 1334–40.
21. N.A.S. Webster, M.I. Pownceby, I.C. Madsen, A.J. Studer, J.R. Manuel, and J.A. Kimpton: *Metall. Mater. Trans. B*, 2014, vol. 45B, pp. 2097–2105.
22. N.A.S. Webster, M.I. Pownceby, R. Pattel, J.R. Manuel, and J.A. Kimpton: *ISIJ Int.*, 2019, vol. 59, pp. 263–67.
23. N.A.S. Webster, M.I. Pownceby, R. Pattel, J.R. Manuel, and J.A. Kimpton: *ISIJ Int.*, 2019, vol. 59, pp. 1007–10.
24. T. Takayama, R. Mura, and M. Kimura: *ISIJ Int.*, 2018, vol. 58, pp. 1069–78.
25. J. Hancart, V. Leroy, and A. Bragard: *CNRM Metall. Rep.*, 1967, vol. 11, pp. 3–7.
26. K. Inoue and T. Ikeda: *Tetsu-to-Hagané*, 1982, vol. 68, pp. 2190–99.
27. P.R. Dawson, J. Ostwald, and K.M. Hayes: *BHP Tech. Bull.*, 1983, vol. 27, pp. 47–51.
28. T.R.C. Patrick and M.I. Pownceby: *Metall. Mater. Trans. B*, 2002, vol. 33B, pp. 79–89.
29. R. Murao, T. Harano, M. Kimura, and I.-H. Jung: *ISIJ Int.*, 2018, vol. 58, pp. 259–66.
30. S. Nicol, J. Chen, M.I. Pownceby, and N.A.S. Webster: *ISIJ Int.*, 2018, vol. 58, pp. 2157–72.
31. H. Guo and X.-M. Guo: *Metall. Mater. Trans. B*, 2018, vol. 49B, pp. 1974–84.
32. J. Chen, M. Shevchenko, P.C. Hayes, and E. Jak: *ISIJ Int.*, 2019, vol. 59, pp. 795–804.
33. T.J. Park, J.S. Choi, and D.J. Min: *Metall. Mater. Trans. B*, 2018, vol. 49B, pp. 2174–81.
34. T.J. Park, J.S. Choi, and D.J. Min: *Metall. Mater. Trans. B*, 2019, vol. 50B, pp. 790–98.
35. S. Nicol, E. Jak, and P.C. Hayes: *Metall. Mater. Trans. B*, 2019, vol. 50B, pp. 2706–22.
36. S. Nicol, E. Jak, and P.C. Hayes: *Metall. Mater. Trans. B*, 2019, vol. 50B, pp. 3027–38.
37. K. Taira and M. Matsumura: *ISIJ Int.*, 2018, vol. 58, pp. 808–14.
38. J.W. Jeon, S.M. Jung, and Y. Sasaki: *ISIJ Int.*, 2010, vol. 50, pp. 1064–70.
39. J. Chen, M. Shevchenko, P.C. Hayes, and E. Jak: *ISIJ Int.*, 2019, vol. 59, pp. 805–09.
40. S.C. Schaefer and R.A. McCune: *Metall. Mater. Trans. B*, 1986, vol. 17B, pp. 515–21.
41. B.F. Decker and J.S. Kasper: *Acta Crystallogr.*, 1957, vol. 10, pp. 332–37.
42. F. Bertaut, P. Blum, and A. Sagnieres: *C. R. Acad. Sci.*, 1957, vol. 244, pp. 2944–46.
43. E. Millon, B. Malaman, A. Bonazebi, J.F. Brice, R. Gerardin, and O. Evrard: *Mater. Res. Bull.*, 1986, vol. 21, pp. 985–94.
44. D.Y. Lee, H.K. Shin, S.M. Moon, W.B. Chung, and W.S. Chung: *J. Kor. Inst. Met. Mater.*, 1996, vol. 34, pp. 387–96.
45. J.H. Park, Y.J. Cho, S.S. Yoon, W.W. Huh, and H.S. Kim: *J. Kor. Inst. Met. Mater.*, 2002, vol. 40, pp. 811–17.
46. S.J. Yoon: *J. Kor. Inst. Met. Mater.*, 2006, vol. 44, pp. 70–76.